Science Advances
AAAS

Manuscript Template

FRONT MATTER

Title

- Coupling Morphological and Magnetic Anisotropy for Assembling Tetragonal Colloidal Crystals
- Magnetic Assembly of Nanorods into Tetragonal Colloidal Crystals

Authors

1. Zhiwei Li[1], Chang Qian[1,†], Wenjing Xu[1], Chenhui Zhu[2], and Yadong Yin[1,*]

Affiliations

[1]Department of Chemistry, University of California, Riverside, CA 92521, USA.

[2]Advanced Light Source, Lawrence Berkeley National Laboratory, 1 Cyclotron Rd, Berkeley, CA 94720, USA.

[*]Corresponding author. Email: yadong.yin@ucr.edu

† Present address: Department of Materials Science and Engineering, University of Illinois at Urbana-Champaign, Urbana, IL 61801, USA

Abstract

Morphological and magnetic anisotropy can be combined in colloidal assembly to create unconventional secondary structures. We show here that magnetite nanorods interact along a critical angle depending on their aspect ratios and assemble into body-centered tetragonal (bct) colloidal crystals. Under a magnetic field, size-dependent attractive and repulsive domains develop on the ends and center of the nanorods, respectively. Our joint experiment-computational multiscale study demonstrates the presence of a critical angle in the attractive domain, which defines the equilibrium bonding states of interacting rods and leads to the formation of non-close-packed yet hard-contact tetragonal crystals. SAXS measurement attributes the perfect tetragonal phase to the slow assembly kinetics. The crystals exhibit brilliant structural colors, which can be actively tuned by changing the magnetic field direction. These highly ordered frameworks and well-defined 3D nanochannels may offer new opportunities for manipulating nanoscale chemical transformation, mass transportation, and wave propagation.

Teaser

Nanorods can be magnetically assembled into tetragonal colloidal crystals along a size-dependent critical angle.

MAIN TEXT

Introduction

Colloidal crystals are ordered superstructures of colloidal particles whose repeating subunits are much larger than their analogous atomic and molecular crystals (*1-4*). The spatial configuration of matter and surface ligands in colloidal crystals, which control many physical and chemical properties, can be tailored in a nanometer precision by adjusting the subunit composites, sizes, shapes, and crystal structures (*5-8*). Therefore, the colloidal assembly has become an effective strategy in producing many functional materials in photonics (*9-12*), structural materials (*13, 14*), robotics (*15-17*), and catalysis (*18, 19*). The assembly of either spherical or highly faceted colloids is mainly dominated by entropic processes that involve depletion, hydrophobic forces, and polymer "elasticity," producing densely packed colloidal crystals with close surface contact (*3, 20, 21*). Theoretical simulations and colloidal self-assembly at multiscale have demonstrated this common assembly manner (*22-24*).

For exploring more complex superstructures, sole or joint anisotropic interactions have been introduced (*25*), including specific binding between biomolecules (particularly DNA) (*26-29*), van der Waals forces of ligands (*1, 30*), magnetic forces (*31-33*), and electrostatic forces (*3, 34, 35*). A few advanced strategies use directed interactions between Janus microparticles for creating emerging superstructures (*36-40*). Among these established methods, the nanoscale magnetic assembly provides precise control over colloidal crystal symmetry and orientation; and the dynamic interplay between magnetic forces and other underlying forces of different length scales offers great opportunities in creating emerging superstructures and smart materials. A great benefit in this regard is the widely accessible range of monodisperse magnetic colloids with defined shapes, tunable properties, and delicate structures. Scientists are achieving even more exquisite control over the synthesis of magnetic particles, including those with various shapes (*41-44*), core/shell nanoparticles (*45-47*), and Janus particles with magnetic patches (*39, 48, 49*), setting the stage ready for exploiting their assembly into complex superstructures with remarkable collective properties. In this work, we demonstrate that body-centered tetragonal (*bct*) superstructures with reduced crystal symmetry can be developed by the magnetic assembly of nanorods in colloidal solutions. It has been known since 1269 that opposite magnetic poles attract, favoring dipole-to-dipole end-on attachment (*50*). At the nanoscale, however, magnetic nanorods assemble along a size-dependent critical angle. The shape-induced anisotropic interaction generates two attractive domains separated by a magnetically repulsive center domain. It directs nanorods to assemble along the critical axis into *bct* crystals, rather than the side-on attachment favored in entropy-dominated assembly or end-on attachment favored by magnet opposite pole attraction. A simple extension of the nanoscale magnetic assembly to different nanorods yields *bct* crystals with tunable lattice constants, tailorable physical properties, readily accessible surfaces, and interconnected nanochannels.

Results

FeOOH nanorods (aspect ratios from 3 to 30) were synthesized by hydrolysis of $FeCl_3$ (**Figs. S1 and S2, Table S1**) and further reduced to magnetic nanorods after being coated with silica of controllable thickness (**Fig. S3**)(*43, 51*). In this surface-protected reduction, the silica shell maintains the rod shape during the phase transition of FeOOH to Fe_3O_4 and alleviates the considerable volume shrinkage. A transmission electron microscopy (TEM) image in **Fig. 1a** reveals the high uniformity of the magnetic rods (322×70 nm). The magnetic assembly was performed by simply sitting a rod dispersion above a permanent magnet with a field strength of 150 mT. As shown in **Figs. 1b, 1c** and **Fig. S4,** stripe-like, green crystals formed. The scanning electron microscope (SEM) image in **Fig. 1c** reveals that the magnetic nanorods are packed into a centered rectangular lattice on the crystal surface. The apparent orthogonality and different periodicity between transverse and longitudinal directions demonstrate the reduced symmetry of the crystals and exclude any triclinic, monoclinic, or cubic crystal systems. These observations suggest a few

possible Bravais lattices, including body-centered orthorhombic, face-centered orthorhombic, and body-centered tetragonal structures.

The silica fixation allows the colloidal crystals to be transformed into other colloid lattices by post-assembly wet chemical processes. For example, selectively etching away Fe_3O_4 yields crystals of SiO_2 shells (**Fig. 1d**). In a 2D projection, the contact joints between neighboring rods form high-density areas (dark regions in the 2D projection) separated by low-density, low-contrast domains (**Figs. S5-S7**). The projection of the assembled crystals along different crystallographic directions produced characteristic 2D TEM images, with two typical lattices being observed, rectangular phase (**Fig. 1e** and **2f**) and centered rectangular phase (**Fig. 1g** and **1h**). In **Fig. 1e,** the periodic empty spaces indicate that the rods are in hard contact but not closely packed. Crystals sharing this characteristic projection have identical transverse periodicity. These observations approve that the assembled structures are body-centered tetragonal (*bct*) crystals since the hard contact between neighboring rods and the same transverse periodicity do not support the different interplanar spacing of (100) and (010) facets in orthorhombic crystals. A high-magnification image of the same area reveals overlaps of rod ends, creating defined joints and interconnected nanometer poles (**Fig. 1f**). In **Fig. 1g and 1h**, we observed layer-by-layer stacking of crystal planes with apparent periodic nodes because of the partial rod overlap. The projection of rod packing along this crystallographic direction is a rectangular 2D lattice. The arrangements of rods in the two typical planes are illustrated in the 2D rendering (**Fig. 1i**). The rods packing in (110) facets is consistent with the SEM images in **Fig. 1c**. The projection patterns (ball-stick bond diagram in **Fig. 1i**) of (100) and (110) facets are consistent with TEM images in **Fig. 1e** and **1f**, respectively.

The rod positions in the crystals are identified and mapped in **Fig. 2a**. Their radical distribution (r_{cc}) in **Fig. 2b** demonstrates the excellent orders and defines the lattice spacing (d) of (110), (100), (101), and (001) facets. The 3D rod arrangement and the crystal rotational symmetry were systematically studied by electron tomography (**Movie S1**). In **Fig. 2c**, we started with a projection of (110) facets, $P_{(110)}$, and acquired TEM images by continuously rotating crystals along [001] and [110] crystallographic directions, denoted as $R_{[001]}$ and $R_{[110]}$, respectively. The initial $P_{(110)}$ exhibits a layer-by-layer structure with a centered rectangular rod packing in (110) facets (**Fig. 2d**). When $R_{[001]}$=45°, we observed a gradual evolution to $P_{(100)}$, with rectangular rod arrangements in (100) facets. In $R_{[110]}$, the initial $P_{(100)}$ transforms to $P_{(111)}$ when the tilting angle increased to 60°, leading to a rectangular out-of-plane topography of rods (**Fig. 2e**). A 3D rendering model and ball-stick bond diagram are illustrated in **Fig. 2f**. In a unit cell, eight rods occupy the vertex sites, with one in the center, forming a *bct* lattice. Its length along the a- and c-axis is 210.6 nm and 513.9 nm, respectively. The angle between [111] and [110] is 30°. Using nanorods with different sizes and silica thicknesses, we obtained several *bct* colloidal crystals with tunable critical angles, lattice constants, and packing densities (**Figs. S8-S14**). In **Fig. 2g**, projections of (100) crystal facets are obtained with rod aspect ratio increasing from 2.25 to 18.5. Due to the dipole-dipole attractions, isotropic nanospheres were assembled into 1D nanochains (*52, 53*). In the phase diagram (inset in **Fig. 2h**), long nanorods (aspect ratio> 20) self-assembled into disordered fibers largely because of the segregation of magnetic cores during reduction.

For Fe_3O_4@SiO_2 colloids with abundant surface charges, the electrostatic repulsion is a major counterforce to the magnetic attraction (*54*). Its classic use involves the multipolar expansion of an analytical equation, whose direction is mainly along the connecting line of interacting colloids. The monopole approximation is operational for isotropic, homogeneously charged spheres (**Fig. S15**) or anisotropic colloids with considerably large separation (*55*). As colloids approach, their morphological anisotropy becomes more effective. Our finite element analysis (**Fig. S16**) points out that the electrostatic repulsion is highly dependent on interparticle separation and that, in closely packed assemblies, it gradually approaches the surface normal of interacting rods. At thermodynamic equilibrium, the tangent component of the magnetic attraction is expected to vanish to avoid any relative translational shifts between nanorods, and the normal component is balanced

by the electrostatic and steric repulsion. For understanding the force dynamics**,** one nanorod (in red color in **Fig. 3a**) is continuously swept along a defined trajectory in hard contact with a primary rod (in blue color). The magnetic force between them is dependent on silica thickness (t) and azimuth angle (Θ) (**Fig. S17** and **Movie S2**). To identify the critical angles (ϕ_c) along which interacting rods thermodynamically equilibrate, we decompose the overall magnetic force into tangent (F_{tang}) and normal components (F_{norm}). In **Fig. 3b**, F_{norm} changes from negative to positive values at Θ=43°, which defines the repulsion and attraction domains, respectively. In the attraction regime, we specify a critical point at F_{tang}=0, where the magnetic attraction is along the surface normal. For 50-nm silica shells, the theoretical ϕ_c is 68.1°, and its good agreement with the measured value of 63.5° from TEM images appreciates the reasonable accuracy of this simple calculation. The normal component in the right panel of **Fig. 3c** demonstrates the presence of the two attractive poles and the repulsive center, with their boundary shifting to small Θ regions as silica thickness increased from 5 to 50 nm. We observed the first decrease and then increase in ϕ_c in the attractive domain (dashed blue line in the left panel of **Fig. 3c**). To understand the deterministic role of aspect ratios, we analyzed ϕ_c for different magnetic rods and map their ϕ_c in a 3D surface in **Fig. 3d**. For isotropic nanospheres, ϕ_c remains 90° due to the dipole-dipole attraction, producing 1D chains with end-on attachment (**Figs. S18 and S19**). Anisotropic nanorods favor offset packing with a defined ϕ_c, which finally degenerate to 90° as the SiO_2 thickness increases. The ϕ_c increased as aspect ratios simply because of rod elongation (**Figs. S20-S27**).

The offset binding between two rods initiated the nucleation of *bct* crystals as neighboring rods assemble at preferential crystalline sites along a predicted critical angle. It likely breaks the lateral symmetry of rods, creating a few preferred sites for rod deposition. The crystal growth features preferential in-plane rod tessellation in {110} facets, as evidenced by contrast differences in TEM images; the uniform contrast of TEM images along <110> projection (**Fig. S28b-d**) implies even, sequent rod packing in the exposed (110) facets. Along <100> (**Fig. S28e-g**) projections, a contrasting gradient implies a gradual decrease of crystal thickness from crystal center to edge. These observations suggest a defined rectangular cross-section of *bct* crystal grains (**Fig. S28a**) and the preferential in-plane rod packing in (110) facets. While the critical angle analysis demonstrates the offset packing of interacting nanorods, the formation of 3D tetragonal crystals requires higher dimension analysis of the assembly dynamics. We extended the force computation to a 3D model (**Figs. S29-S32 and Movie S3**). The force field in **Fig. 3e** suggests a strong repulsion (red arrows) when the rod overlaps the bottom ones. We observe a gradual shift to a strong attraction when the rod moves to positions above cavities (blue arrows). In the magnetic potential landscape (**Fig. 3f**), we recognize periodic bonding sites above bottom cavities due to the localized low magnetic potential. There exist four active sites above and below each rod in the 2D sheet, resulting in eight bonded rods shared by its neighbors.

To resolve the assembly kinetics, we analyzed the crystallization by *in situ* synchrotron-based small-angle X-ray scattering (SAXS) based on the geometry shown in **Fig. S33** (*56*). The representative 2D SAXS patterns are shown in **Figs. 4a, S34, and Movie S4**. At 0 min, the anisotropic scattering pattern implies the liquid crystal phase of rods with only orientational orders and parallel alignment to a vertical magnetic field. At 33 min, a defined rectangular diffraction pattern appeared as nanorods began to crystalize, which is the reciprocal lattice of {110} facets (**Fig. S35**). The high-order diffraction peaks confirm the perfect structures of the bct crystals. For example, the linear profiles in **Fig. 4b** (horizontal) and **4c** (vertical) show a 9th diffraction of {110} facets and 5th diffraction of {001} facets, respectively. **Fig. 4d** represents a time-dependent contraction of the lattice under external magnetic fields with exponential superlattice densification. The lattice contraction rate along both the a and c directions was initially at ~4 nm/min and slowed down when approaching thermodynamic equilibrium at ~90 min. The considerably slow assembly kinetics provide rods with sufficient spatiotemporal degrees of freedom to anneal out defects. **Fig. 4e** shows the evolution of local rod position along <111> crystallographic directions, indicating

nearly linear spatial lattice contraction (**Fig. S36**). The overall magnetic assembly was compiled and depicted in **Fig. 4f** with lattice shrinkage of 31.7% and 22.4% for a and c axis, respectively.

The *bct* crystals exhibit brilliant structural colors that are dependent on crystal orientation (**Movie S5**). In the dark-field optical microscopy images in **Fig. 5a**, we observed structural colors diffracted from two types of facets: red from {110} and green from {100} facets. The uniform structural colors elucidate the good crystallinity of the superstructures. The incident light was kept vertical along the crystal surface for measuring the angle-dependent optical properties (**Fig. 5b**). A horizontal magnetic field (0°) was applied, and spectra were measured by gradually changing the field to the vertical direction (90°). The three primary colors, blue, green, and red, can be observed at 0°, 20 °, and 45°, respectively (**Fig. 5c**). The diffraction spectra in **Fig. 5d** further demonstrated a gradual redshift of the diffraction peaks because of the increasing periodicity when the crystal orientation increased to 90°. Their diffraction could cover the whole visible range from blue to cyan, green, yellow, orange, and finally red by simply changing the magnetic field directions (**Fig. 5e, Movie S6 and S7**). A simple extension to different nanorods yields photonic crystals with tunable lattice constants and structure colors (**Fig. S37**).

Discussion

In summary, we report the magnetic assembly of magnetite nanorods into tetragonal colloidal crystals and show that the magnetic nanorods assemble along a size-dependent critical angle rather than the simple end-on attachment. The coupled shape and magnetic anisotropy in nanorods is responsible for the unconventional assembly manner and leads to the non-close packed and hard contact phase. The unique 3D tetragonal architectures and tunable, interconnected porosity provide a unique platform to modulate many chemical transformations and physical processes in energy conversion and optical devices. This work demonstrates that manipulating magnetic interactions of various anisotropically shaped nanostructures can break the limitation of the dense packing phase in the conventional entropy-dominated colloidal assembly systems, thereby opening the door to creating many complex colloidal crystals.

Materials and Methods

Synthesis of FeOOH nanorods.

The synthesis of nanorods with different aspect ratios was achieved by hydrolysis of $FeCl_3$ in an aqueous solution (*57, 58*). The details about the concentration and reaction temperature are summarized in **Table. S1**. The synthesis of FeOOH nanorods with small aspect ratios was carried out at room temperature without HCl. Due to relatively low temperature, it takes about 3 months for the formation of uniform FeOOH nanorods. To synthesize FeOOH nanorods with larger aspect ratios (**Fig. S2**), we added HCl to the solution and raised the reaction temperature to 87°C. The reactions were kept at this temperature for 25.5 hours. Notably, this hydrolysis method can be easily scaled up without a significant change in size and aspect ratios. In the example of rods with aspect ratios of 4.6 (#F2), the total volume was 4 L during room-temperature hydrolysis. The concentration of $FeCl_3 \cdot 6H_2O$ is 0.04 M. During the reaction, the formed FeOOH nanorods precipitated to the bottom of the reaction containers. After removing the supernatants, the FeOOH nanorods were washed by water three times and then dispersed in 400 mL of water, which served as stock solutions.

PAA modification.

For PAA modification, 3 mL of the stock solution with a theoretical concentration of 90 mg/mL was added into 120 mL of PAA solution (43.2 mg) and stirred for 8 hrs. Excess PAA was removed by centrifugation and washing with water three times. The FeOOH-PAA was further dispersed in 9 mL of water for SiO_2 coating.

SiO_2 coating. In a typical coating process, 3 mL of FeOOH-PAA dispersion was added into a flask. The mixture was sonicated for 3 min to fully disperse the rods after 1 mL of ammonia solution was added. Then, 20 mL of ethanol was added to the dispersion. To control the thickness of silica, we

added different volumes of TEOS to the mixture. In #F2, for example, 30 μL and 100 μL of TEOS were added to the mixture to achieve thicknesses of 20.5 and 44.2 nm, respectively, after a 30 min reaction. For thicker silica (~ 72.8 nm), two batches of 130 μL TEOS were added to the mixture each 30 min to prevent the formation of free silica nanoparticles. Half an hour after the second addition, the FeOOH@SiO_2 nanorods were precipitated by centrifugation and further washed three times by water.

High-temperature reduction.

Magnetic nanorods were synthesized by reduction of FeOOH@SiO_2 nanorods in high-temperature calcination. FeOOH@SiO_2 nanorods were dried in crucibles and placed in a tubular furnace (**Fig. S3**). The system was de-gassed for 10 min by forming gas (5% H_2 and 95% N_2). The reduction occurred at 360ºC for 2 hours. After cooling down to room temperature, the prepared Fe_3O_4@SiO_2 nanorods were fully dispersed in water by sonication and then washed by water three times. To further increase the surface charges and facilitate the fixation of colloidal crystals by silica coating, the Fe_3O_4@SiO_2 nanorods were modified by PAA (20mL, 5 mg/mL) overnight.

Magnetic assembly of nanorods into tetragonal crystals

The assembly of colloidal crystals took place in aqueous dispersions of Fe_3O_4@SiO_2 nanorods (**Fig. S4**). The dispersion was vertically placed above the center of a permanent magnet. For measuring the diffraction of the crystals, colloidal dispersion of Fe_3O_4@SiO_2 nanorods with an initial volume fraction of ~45% was sealed in a flat capillary. After assembling under the magnetic field, diffraction spectra were measured by continuously varying the directions of the applied magnetic field, and the pictures were also taken at the corresponding angles (**Fig. 5C**). To fix the assembled crystals, we used a small well of the 96 well plates as the container. In a typical reaction, 25 μL of an aqueous dispersion of Fe_3O_4@SiO_2 nanorods (volume fraction of ~45%) was transferred into the well. 3 μL of ammonia, 100 μL of ethanol, and 10 μL of TEOS were added in sequence. The mixture was sonicated for ~ 30s and then placed above a permanent magnet. Additional 3 μL of ammonia was added after 10 min, and the reaction was continued for another 10 min. The precipitated crystals were washed with ethanol three times. During each cycle of washing, the crystals were collected by magnetic separation. Sonication and centrifugation would destroy the fixed crystal structures and therefore are not recommended. The crystals were stored in ethanol for further characterization. The positional order of the colloidal crystals decayed because long nanorods were synthesized in high-temperature hydrolysis, and the relatively fast crystal growth produces widely dispersed particles. More TEM images of the bct crystals are shown in **Fig. S5**. According to the projection patterns, we typically observed two types of crystal orientations. Fixing neighboring rods by silica overcoating imparts considerable mechanical stability to the crystals, as demonstrated by twisting and bending the *bct* crystals under mechanical forces (**Fig. S6**). Instead of being destroyed, the crystals deformed to release the internal strains, exhibiting interesting, combined states of colloid rigidness and mechanical elasticity.

References

1. T. Wang, J. Zhuang, J. Lynch, O. Chen, Z. Wang, X. Wang, D. LaMontagne, H. Wu, Z. Wang, Y. C. Cao, Self-assembled colloidal superparticles from nanorods. *Science* **338**, 358-363 (2012).
2. F. Li, D. P. Josephson, A. Stein, Colloidal assembly: the road from particles to colloidal molecules and crystals. *Angew. Chem. Int. Ed.d.* **50**, 360-388 (2011).
3. W. Xu, Z. Li, Y. Yin, Colloidal assembly approaches to micro/nanostructures of complex morphologies. *Small* **14**, 1801083 (2018).
4. Z. Cai, Z. Li, S. Ravaine, M. He, Y. Song, Y. Yin, H. Zheng, J. Teng, A. Zhang, From colloidal particles to photonic crystals: advances in self-assembly and their emerging applications. *Chem. Soc. Rev.* **50**, 5898-5951 (2021).

5. Z. Li, Y. Yin, Stimuli-responsive optical nanomaterials. *Adv. Mater.* **31**, 1807061 (2019).
6. S. C. Glotzer, M. J. Solomon, Anisotropy of building blocks and their assembly into complex structures. *Nat. Mater.* **6**, 557-562 (2007).
7. S. Sacanna, D. J. Pine, Shape-anisotropic colloids: Building blocks for complex assemblies. *Curr. Opin. Colloid Interface Sci.* **16**, 96-105 (2011).
8. D. V. Talapin, J.-S. Lee, M. V. Kovalenko, E. V. Shevchenko, Prospects of colloidal nanocrystals for electronic and optoelectronic applications. *Chem. Rev.* **110**, 389-458 (2010).
9. J. Ge, Y. Yin, Responsive photonic crystals. *Angew. Chem. Int. Ed.* **50**, 1492-1522 (2011).
10. Z. Li, Q. Fan, C. Wu, Y. Li, C. Cheng, Y. Yin, Magnetically Tunable Plasmon Coupling of Au Nanoshells Enabled by Space-Free Confined Growth. *Nano Lett.* **20**, 8242-8249 (2020).
11. G. von Freymann, V. Kitaev, B. V. Lotsch, G. A. Ozin, Bottom-up assembly of photonic crystals. *Chem. Soc. Rev.* **42**, 2528-2554 (2013).
12. Z. Li, W. Wang, Y. Yin, Colloidal Assembly and Active Tuning of Coupled Plasmonic Nanospheres. *Trends Chem.* **2**, 593-608 (2020).
13. H.-B. Yao, H.-Y. Fang, X.-H. Wang, S.-H. Yu, Hierarchical assembly of micro-/nano-building blocks: bio-inspired rigid structural functional materials. *Chem. Soc. Rev.* **40**, 3764-3785 (2011).
14. Z. Li, F. Yang, Y. Yin, Smart materials by nanoscale magnetic assembly. *Adv. Funct. Mater.* **30**, 1903467 (2020).
15. Y. Wang, H. Cui, Q. Zhao, X. Du, Chameleon-inspired structural-color actuators. *Matter* **1**, 626-638 (2019).
16. Z. Li, Z. Ye, L. Han, Q. Fan, C. Wu, D. Ding, H. L. Xin, N. V. Myung, Y. Yin, Polarization-modulated multidirectional photothermal actuators. *Adv. Mater.* **33**, 2006367 (2021).
17. Y. Kim, H. Yuk, R. Zhao, S. A. Chester, X. Zhao, Printing ferromagnetic domains for untethered fast-transforming soft materials. *Nature* **558**, 274-279 (2018).
18. G. M. Whitesides, B. Grzybowski, Self-assembly at all scales. *Science* **295**, 2418-2421 (2002).
19. K. Li, K. Wang, W. Qin, S. Deng, D. Li, J. Shi, Q. Huang, C. Fan, DNA-directed assembly of gold nanohalo for quantitative plasmonic imaging of single-particle catalysis. *J. Am. Chem. Soc.* **137**, 4292-4295 (2015).
20. P. F. Damasceno, M. Engel, S. C. Glotzer, Crystalline assemblies and densest packings of a family of truncated tetrahedra and the role of directional entropic forces. *Acs Nano* **6**, 609-614 (2011).
21. W. Han, Z. Lin, Learning from "Coffee Rings": Ordered Structures Enabled by Controlled Evaporative Self-Assembly. *Angew. Chem. Int. Ed.d.* **51**, 1534-1546 (2012).
22. P. F. Damasceno, M. Engel, S. C. Glotzer, Predictive self-assembly of polyhedra into complex structures. *Science* **337**, 453-457 (2012).
23. J. Henzie, M. Grünwald, A. Widmer-Cooper, P. L. Geissler, P. Yang, Self-assembly of uniform polyhedral silver nanocrystals into densest packings and exotic superlattices. *Nat. Mater.* **11**, 131-137 (2012).
24. E. V. Shevchenko, D. V. Talapin, N. A. Kotov, S. O'Brien, C. B. Murray, Structural diversity in binary nanoparticle superlattices. *Nature* **439**, 55-59 (2006).
25. Z. Ou, Z. Wang, B. Luo, E. Luijten, Q. Chen, Kinetic pathways of crystallization at the nanoscale. *Nat. Mater.* **19**, 450-455 (2020).
26. R. J. Macfarlane, B. Lee, M. R. Jones, N. Harris, G. C. Schatz, C. A. Mirkin, Nanoparticle superlattice engineering with DNA. *Science* **334**, 204-208 (2011).

27. S. Y. Park, A. K. Lytton-Jean, B. Lee, S. Weigand, G. C. Schatz, C. A. Mirkin, DNA-programmable nanoparticle crystallization. *Nature* **451**, 553-556 (2008).
28. E. Auyeung, T. I. Li, A. J. Senesi, A. L. Schmucker, B. C. Pals, M. O. de La Cruz, C. A. Mirkin, DNA-mediated nanoparticle crystallization into Wulff polyhedra. *Nature* **505**, 73 (2014).
29. H. Lin, S. Lee, L. Sun, M. Spellings, M. Engel, S. C. Glotzer, C. A. Mirkin, Clathrate colloidal crystals. *Science* **355**, 931-935 (2017).
30. X. Ye, J. Chen, M. Engel, J. A. Millan, W. Li, L. Qi, G. Xing, J. E. Collins, C. R. Kagan, J. Li, Competition of shape and interaction patchiness for self-assembling nanoplates. *Nat. Chem.* **5**, 466-473 (2013).
31. G. Singh, H. Chan, A. Baskin, E. Gelman, N. Repnin, P. Král, R. Klajn, Self-assembly of magnetite nanocubes into helical superstructures. *Science* **345**, 1149-1153 (2014).
32. R. M. Erb, H. S. Son, B. Samanta, V. M. Rotello, B. B. Yellen, Magnetic assembly of colloidal superstructures with multipole symmetry. *Nature* **457**, 999-1002 (2009).
33. Q. Zhang, M. Janner, L. He, M. Wang, Y. Hu, Y. Lu, Y. Yin, Photonic labyrinths: Two-dimensional dynamic magnetic assembly and in situ solidification. *Nano Lett.* **13**, 1770-1775 (2013).
34. M. Wang, L. He, W. Xu, X. Wang, Y. Yin, Magnetic assembly and field-tuning of ellipsoidal-nanoparticle-based colloidal photonic crystals. *Angew. Chem. Int. Ed.d.* **54**, 7077-7081 (2015).
35. M. E. Leunissen, C. G. Christova, A.-P. Hynninen, C. P. Royall, A. I. Campbell, A. Imhof, M. Dijkstra, R. Van Roij, A. Van Blaaderen, Ionic colloidal crystals of oppositely charged particles. *Nature* **437**, 235-240 (2005).
36. Q. Chen, S. C. Bae, S. Granick, Directed self-assembly of a colloidal kagome lattice. *Nature* **469**, 381-384 (2011).
37. A. A. Shah, B. Schultz, W. Zhang, S. C. Glotzer, M. J. Solomon, Actuation of shape-memory colloidal fibres of Janus ellipsoids. *Nat. Mater* **14**, 117-124 (2015).
38. Q. Chen, J. K. Whitmer, S. Jiang, S. C. Bae, E. Luijten, S. Granick, Supracolloidal reaction kinetics of Janus spheres. *Science* **331**, 199-202 (2011).
39. S. K. Smoukov, S. Gangwal, M. Marquez, O. D. Velev, Reconfigurable responsive structures assembled from magnetic Janus particles. *Soft Matter* **5**, 1285-1292 (2009).
40. A. Walther, A. H. Muller, Janus particles: synthesis, self-assembly, physical properties, and applications. *Chem. Rev.* **113**, 5194-5261 (2013).
41. Z. Li, M. Wang, X. Zhang, D. Wang, W. Xu, Y. Yin, Magnetic assembly of nanocubes for orientation-dependent photonic responses. *Nano Lett.* **19**, 6673-6680 (2019).
42. Y. Liu, J. Wang, M. Zhang, H. Li, Z. Lin, Polymer-Ligated Nanocrystals Enabled by Nonlinear Block Copolymer Nanoreactors: Synthesis, Properties, and Applications. *ACS nano* **14**, 12491-12521 (2020).
43. W. Xu, M. Wang, Z. Li, X. Wang, Y. Wang, M. Xing, Y. Yin, Chemical transformation of colloidal nanostructures with morphological preservation by surface-protection with capping ligands. *Nano Lett.* **17**, 2713-2718 (2017).
44. J. Ge, Y. Hu, M. Biasini, W. P. Beyermann, Y. Yin, Superparamagnetic magnetite colloidal nanocrystal clusters. *Angew. Chem. Int. Ed.d.* **46**, 4342-4345 (2007).
45. X. Pang, L. Zhao, W. Han, X. Xin, Z. Lin, A general and robust strategy for the synthesis of nearly monodisperse colloidal nanocrystals. *Nat. Nanotechnol.* **8**, 426-431 (2013).
46. X. Pang, Y. He, J. Jung, Z. Lin, 1D nanocrystals with precisely controlled dimensions, compositions, and architectures. *Science* **353**, 1268-1272 (2016).
47. D. Yang, X. Pang, Y. He, Y. Wang, G. Chen, W. Wang, Z. Lin, Precisely Size-Tunable Magnetic/Plasmonic Core/Shell Nanoparticles with Controlled Optical Properties. *Angew. Chem. Int. Ed.* **41**, 12091-12096 (2015).

48. Q. Xie, G. B. Davies, J. Harting, Direct assembly of magnetic Janus particles at a droplet interface. *ACS nano* **11**, 11232-11239 (2017).
49. J. Hu, S. Zhou, Y. Sun, X. Fang, L. Wu, Fabrication, properties and applications of Janus particles. *Chem. Soc. Rev.* **41**, 4356-4378 (2012).
50. P. Peregrinus, *The Letter of Petrus Peregrinus on the Magnet, AD 1269*. (Library of Alexandria, 2020), vol. 1.
51. Y. Lu, Y. Yin, B. T. Mayers, Y. Xia, Modifying the surface properties of superparamagnetic iron oxide nanoparticles through a sol− gel approach. *Nano Lett.* **2**, 183-186 (2002).
52. J. Ge, Y. Hu, Y. Yin, Highly Tunable Superparamagnetic Colloidal Photonic Crystals. *Angew. Chem. Int. Ed.* **46**, 7428-7431 (2007).
53. Y. Hu, L. He, Y. Yin, Magnetically Responsive Photonic Nanochains. *Angew. Chem. Int. Ed.* **50**, 3747-3750 (2011).
54. L. He, M. Wang, J. Ge, Y. Yin, Magnetic assembly route to colloidal responsive photonic nanostructures. *Acc. Chem. Res.* **45**, 1431-1440 (2012).
55. H. N. Lekkerkerker, R. Tuinier, *Colloids and the depletion interaction*. (Springer, 2011), vol. 833, pp. 57-108.
56. A. Hexemer, W. Bras, J. Glossinger, E. Schaible, E. Gann, R. Kirian, A. MacDowell, M. Church, B. Rude, H. Padmore, A SAXS/WAXS/GISAXS beamline with multilayer monochromator. *J. Phys. Conf. Ser.* **247**, 012007 (2010).
57. X. Wang, J. Feng, H. Yu, Y. Jin, A. Davidson, Z. Li, Y. Yin, Anisotropically shaped magnetic/plasmonic nanocomposites for information encryption and magnetic-field-direction sensing. *Research* **2018**, 7527825 (2018).
58. Z. Li, J. Jin, F. Yang, N. Song, Y. Yin, Coupling magnetic and plasmonic anisotropy in hybrid nanorods for mechanochromic responses. *Nat. Commun.* **11**, 2883 (2020).
59. J. Ilavsky, Nika: software for two-dimensional data reduction. *J. Appl. Crystallogr.* **45**, 324-328 (2012).
60. J. Ilavsky, P. R. Jemian, Irena: tool suite for modeling and analysis of small-angle scattering. *J. Appl. Crystallogr.* **42**, 347-353 (2009).

Acknowledgments

The authors are grateful for the financial support from the U.S. National Science Foundation (DMR-1810485). Li thanks Xiaojing Wang for helpful discussion in nanorod synthesis and Qingsong Fan in theoretical analysis. This research used beamline 7.3.3 of the Advanced Light Source, which is a DOE Office of Science User Facility under contract no. DE-AC02-05CH11231. Acknowledgment is also made to the Central Facility for Advanced Microscopy and Microanalysis at UCR for help with TEM analysis.

Funding:
National Science Foundation DMR-1810485

Author contributions:

Conceptualization: ZWL, YDY
Methodology: ZWL, CQ
Investigation: ZWL, WJX, CHZ
Supervision: YDY
Writing—original draft: ZWL
Writing—review & editing: YDY

Competing interests: YDY and ZWL have filed a patent application covering the magnetic assembly of nanorods into tetragonal photonic crystals. All other authors declare they have no competing interests.

Data and materials availability: All data needed to evaluate the conclusions in the paper are present in the paper and/or the Supplementary Materials. Additional dataset used to analyze the critical angles, phase diagram, electrostatic forces, and magnetic forces are available online at https://zenodo.org/record/4950032#.YMqqbvKSk2w.

Figures and Tables

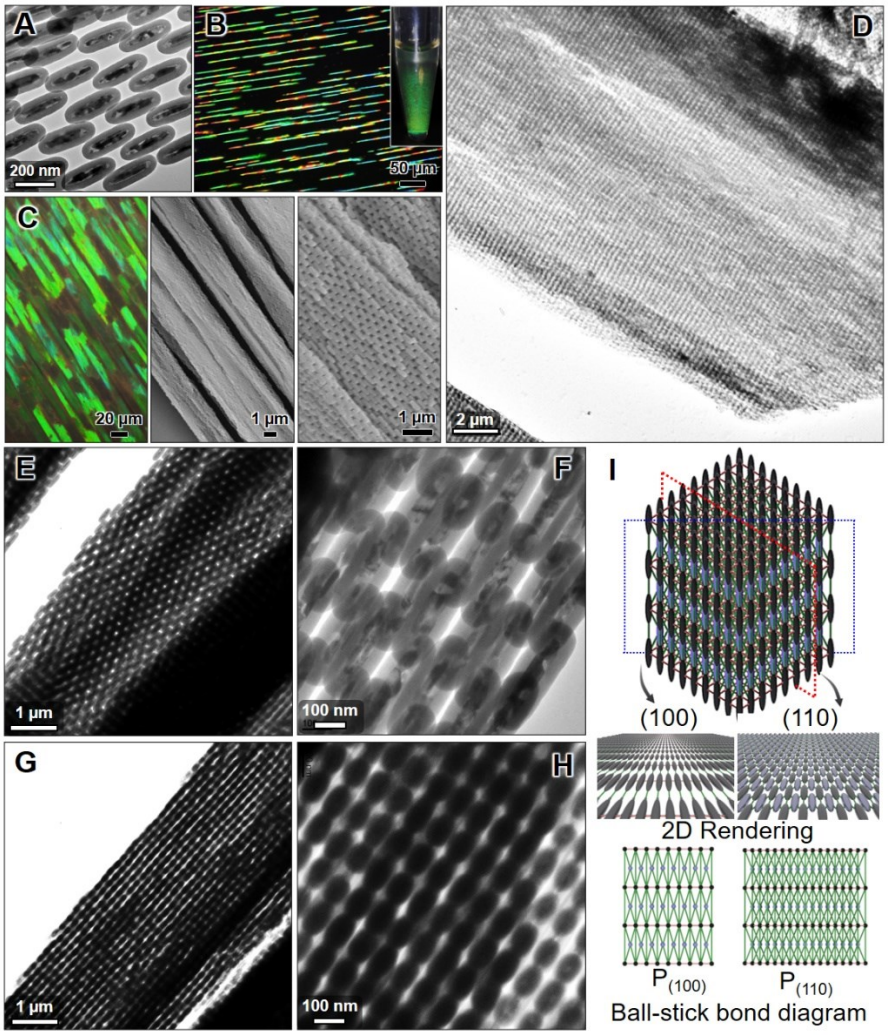

Fig. 1. Magnetic assembly of nanorods into *bct* colloidal crystals. (**A**) TEM image of Fe_3O_4@SiO_2 nanorods. (**B**) Dark-field optical microscopy image of the needle-like colloidal crystals under an external magnetic field. Inset shows a digital photo of a rod dispersion in a vertical magnetic field. (**C**) Left: Optical microscopy image of the colloidal crystals in a colloidal dispersion. Middle to right: low-magnification SEM image showing the fixed needle-like structures and high-magnification SEM image showing the characteristic rod packing on the crystal surfaces. (**D**) Low-magnification TEM image of assembled hollow SiO_2 ellipsoids formed by post-assembly etching of Fe_3O_4 core. (**E-H**) TEM images of the assembled crystals under the projections of different crystal facets. (**I**) The 3D reddening and ball-stick bond diagram of the *bct* colloidal crystal and its facets.

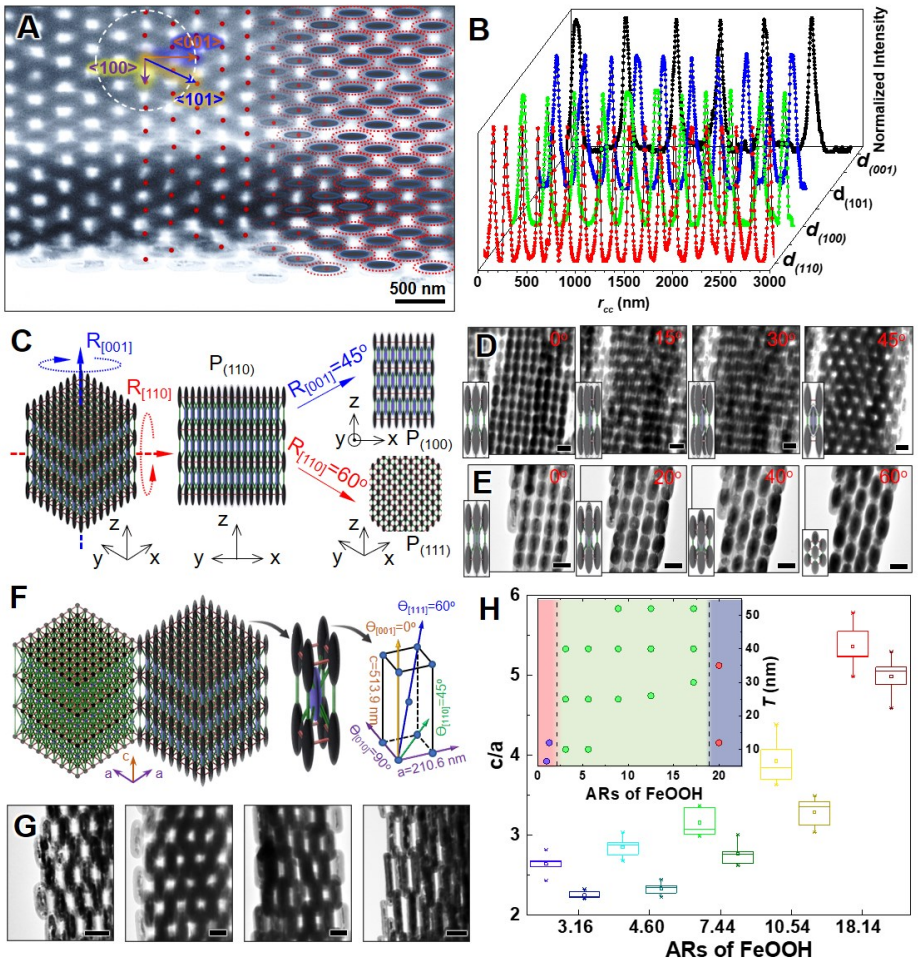

Fig. 2. Structure characterization of *bct* colloidal crystals. (**A**) TEM image of the *bct* crystal showing the projection of (100) facets. Positions of rods are identified and mapped to a *bct* lattice. (**B**) Normalized distribution intensity of nanorods inside the crystals in (**A**) along different crystallographic directions. (**C**) Schematics of *bct* crystals under different orientations by rotating along given crystallographic directions. TEM images in (**D**) and (**E**) show *bct* crystals under various orientations by rotating along [001] and [110], respectively. (**F**) Simulated *bct* colloidal crystals. (**G**) TEM images of *bct* crystals assembled from magnetic nanorods with different sizes and aspect ratios. (**H**) The dependence of lattice constant ratio (c/a) on the aspect ratio of magnetic nanorods. Inset is the experimental phase diagram showing the magnetic assembly behaviors of rods. Blue, green, and red dots represent linear colloidal chains, *bct* crystals, and disordered fibers with only orientational orders, respectively.

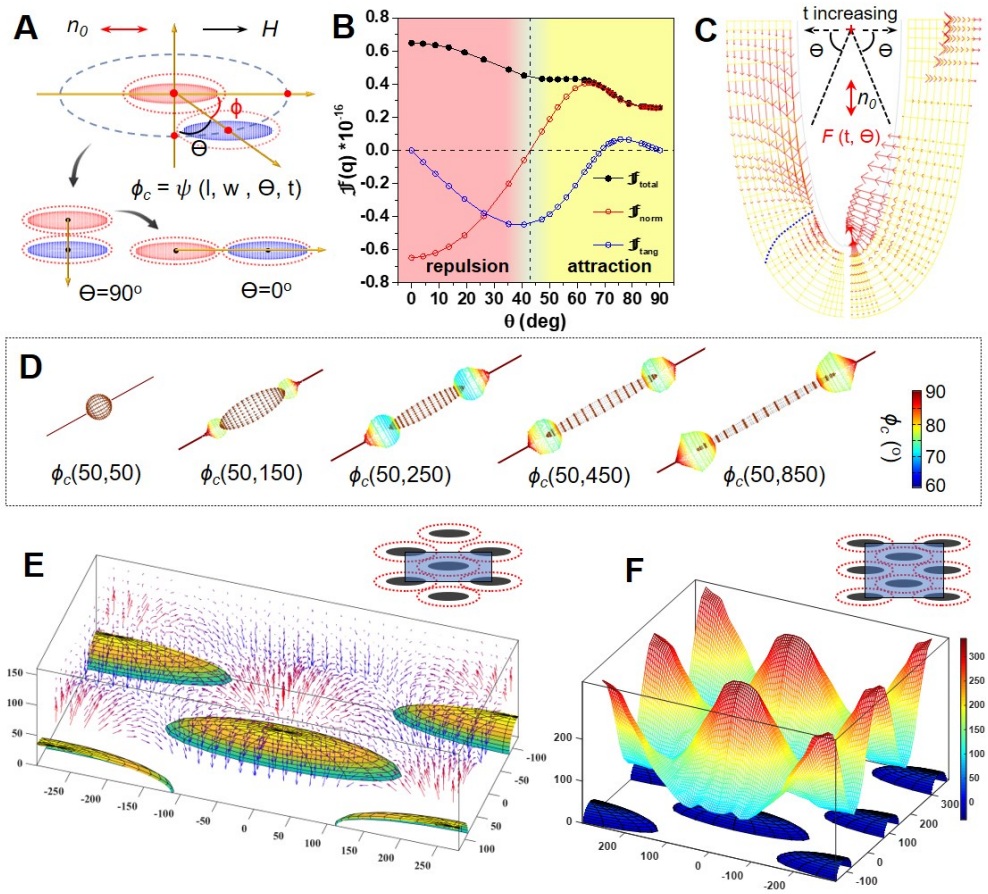

Fig. 3. Assembly mechanism and force dynamics. (**A**) Schematics showing the geometry for calculating the pair interaction between two nanorods under a horizontal magnetic field. (**B**) Plot of total force and its normal, tangent components against Θ when SiO_2 thickness is 50 nm. (**C**) Force field of the normal (left half) and tangent (right half) components of the pair interactions between two magnetic nanorods (t= 50 nm) by varying separation and angles (Θ) between r_{cc} and n_0. (**D**) 3D mapping of critical angles (ϕ_c) for nanorods with different aspect ratios. (**E**) 3D force fields of magnetic interactions experienced by one nanorod above the 2D assemblies. (**F**) Magnetic potential above the 2D assemblies at certain separations.

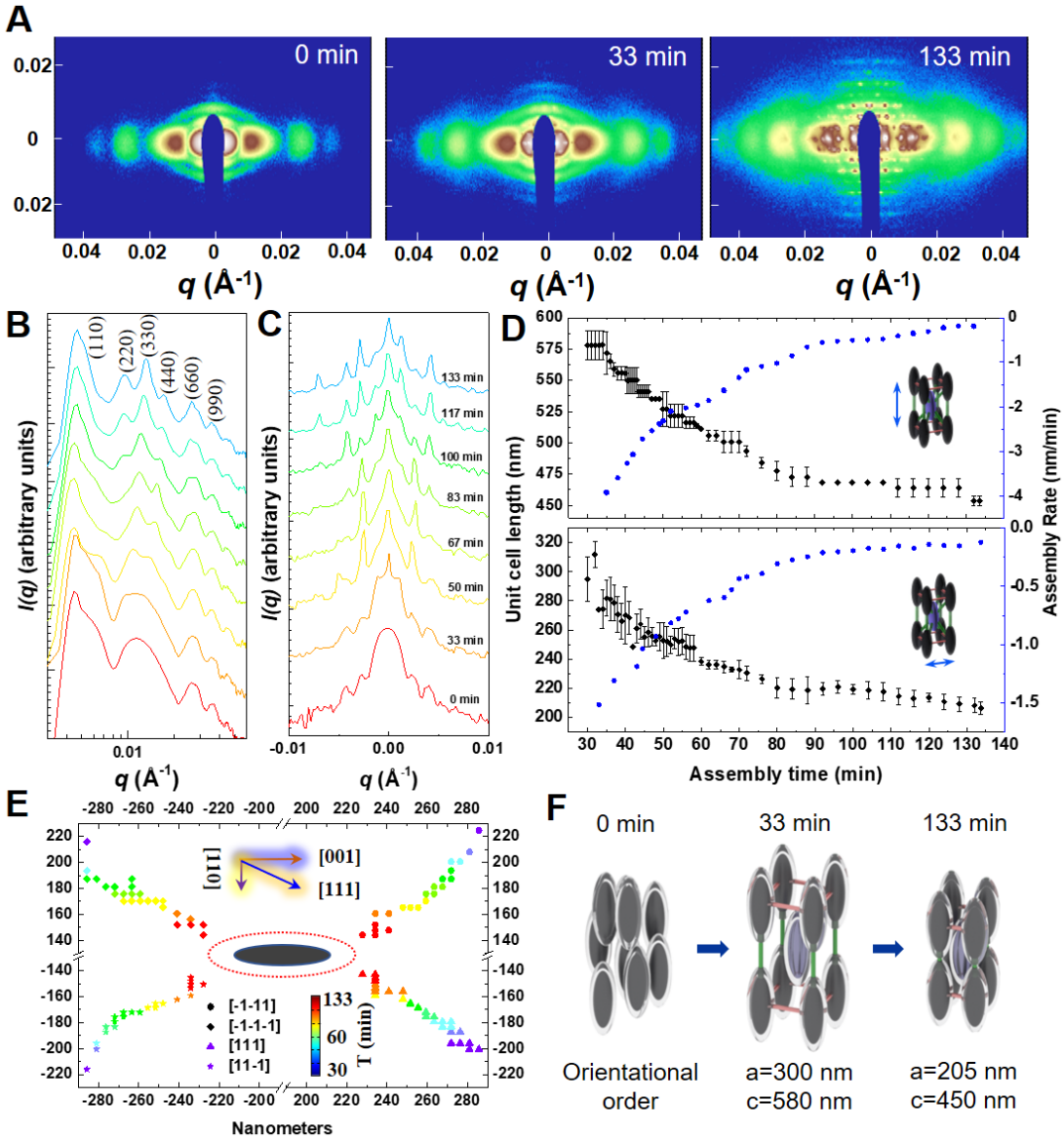

Fig. 4. Assembly kinetics. (**A**) Temporal evolution of SAXS patterns during the *in-situ* measurement of magnetic assembly of nanorods**.** (**B-C**) Representative linear profile of SAXS patterns along the horizontal (**B**) and vertical (**C**) directions. (**D**) Magnetic assembly kinetics of the *bct* crystals along c-axis (top) and a-axis (bottom). (**E**) The trajectory of the magnetic nanorods during the assembly process. (**F**) The depiction of the magnetic assembly and formation of *bct* crystals.

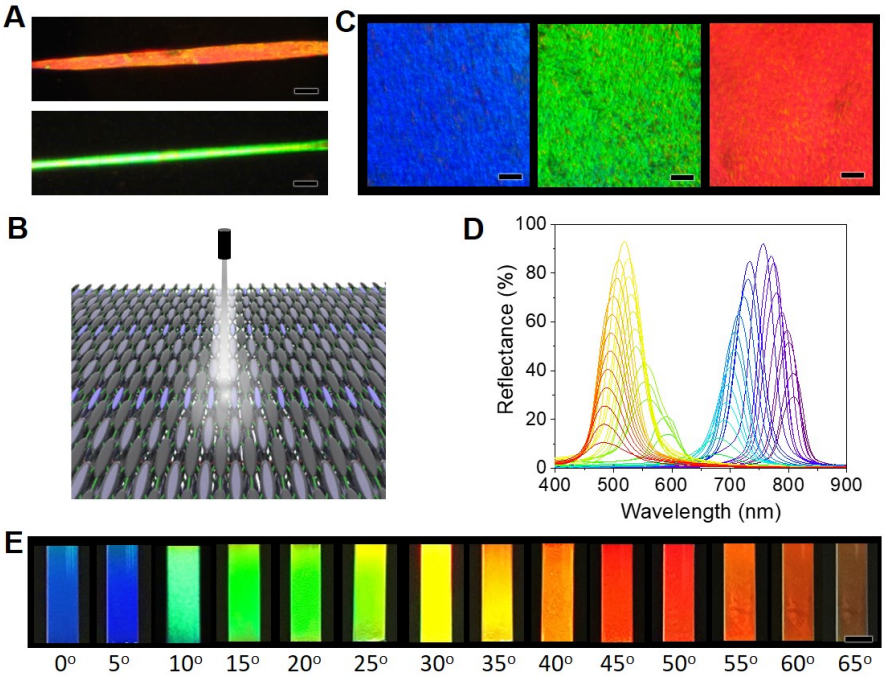

Fig. 5. Optical properties of the assembled *bct* photonic crystals. (**A**) Optical microscopy images of a *bct* crystal under different orientations. (**B**) Schematic illustration of measuring the crystal optical properties. Light was incident along the surface normal, and a horizontal (0°) magnetic field was applied. (**C**) Optical microscopy images of the *bct* crystals under different magnetic field directions: blue at 0°, green at 20°, and red at 45°. (**D**) Measured reflection spectra of rod dispersion under different magnetic fields. Increasing the field direction from 0° to 65° leads to a gradual redshift of the reflection peaks. (**E**) Structural colors of rods dispersion under different magnetic fields. Scale bars: 20 μm in (**A**) and (**C**); 5 mm in (**E**).